Antenna effect of 2-thenoyltrifluoroacetone (TTA) on the luminescence of Y_2O_3 co-doped with Eu^{3+};Tb^{3+}

A.D. Alcantar-Mendoza, F.J. Carrillo-Romo, A. García-Murillo, M. Diaz-Cruz, M.R. González-García

Y_2O_3 gels co-doped with lanthanide ions (Ln^{3+}) were synthesized based on the sol-gel process. Eu^{3+} was used in proportions of 2, 4, and 8 mol% and Tb^{3+} at a low and constant concentration of 0.075 mol% (Y_2O_3:Eu^{3+};Tb^{3+}). The gels were subjected to supercritical drying (aerogel) at 73 bar and 34 °C and to thermal treatment at 800 °C to obtain crystalline materials (crystallized aerogels). Subsequently, each sample was sensitized in a novel way with 9 µmol of the compound 2-thenoyltrifluoroacetone (TTA) -- Y_2O_3:Eu^{3+};Tb^{3+}/TTA, to provide an antenna effect in order to focus the morphological, structural-chemical, and luminescent changes assigned to the energy transitions of Eu^{3+}. When the crystal structure by X-ray diffraction (XRD) and the morphology by scanning electron microscopy (SEM) were analyzed, no drastic changes due to functionalization were observed. However, infrared (IR) and Raman spectroscopies were performed to identify the rare-earth oxides vibrational modes, although its main function was to reveal the adhesion of TTA to materials. The excitation-emission spectra were studied to evaluate the energy transfer to the Eu^{3+} activator ion and the influence of both the Tb^{3+} sensitizer and the TTA ligand on the luminescent properties of the samples Y_2O_3:Eu^{3+};Tb^{3+} and Y_2O_3:Eu^{3+};Tb^{3+}/TTA, also the quantum yield corresponding to the highest luminescence samples was calculated. Based on the results, this class of materials can have novel and useful applications when TTA functionalization is fully exploited.

Introduction

In recent years, materials synthesized from rare-earth oxides (REOs) with nanometric characteristics have presented great benefits due to physical, chemical, and structural properties that they have due to the increase in contact with the surface area [1-3]. Some of the applications of REOs materials are in areas of great relevance today where their optical properties can be exploited; they can be used in display devices [4], light-emitting diodes (LEDs) [5], authentication systems [6], lasers [7], sensors [8], biomarkers or phototherapy [9], among other applications [10,11].

To date, there are different methods of synthesis for the production of new and improved REOs materials. One of the most-used, due to the advantages of its processes and the diversity in the final forms of materials it can yield, is the sol-gel synthesis [12-14]. More and more variants of this method are emerging to expand the established routes for obtaining materials such as dense ceramics, thin films and coatings, precipitated particles, dispersed particles, or aerogels [15,16].

Particularly, aerogels are synthetic solids with the highest porosity ever achieved; they make excellent insulating or absorbent materials. In the manufacture of these materials, from a gel composed of a liquid phase and a solid phase [17,18], the first of them phases is extracted in such a way that their microstructure consists of a 3D network of interconnected particles surrounded by a large number of pores [19,20]. However, one of the reasons they have been slow to be taken up and exploited at an industrial level is that the methods and research for their production are usually expensive and limited to obtaining the material after supercritical drying [21], this limits its applications; however, there may be options to subject them to secondary or even tertiary processes, with the aim of enhancing the properties of aerogels, making them more innovative and attractive for the industry [22].

Figure 1 shows a general diagram for the production of aerogels, in which a metal salt is used to obtain a sol, from which, through hydrolysis and condensation reactions, a gel is produced. This is the basic principle of this synthesis method, as its name indicates [23-25]. Once a wet gel that can be manipulated without flowing is obtained, supercritical drying is performed based on the characteristics of the solvent used in the synthesis to obtain an aerogel (Figure 1a) [26,27]. One variant of the method that has been tested produces crystalline aerogels using thermal treatment, although this step can collapse the aerogel and contract its structure (Figure 1b) [28-30]. If the process is successful, the resulting crystallized aerogel will have new properties resulting from the formation of crystalline structures. However, there is another possibility, which is to functionalize the crystallized aerogel to form a complex/hybrid/functionalized material with modified properties (Figure 1c).

At present, yttrium oxide (Y_2O_3) has been considerably studied and synthesized by sol-gel methods as a promising compound for use in alloying material, refractory material, biological applications, laser crystals, and luminescent matrices [31-33]. Doping or co-doping with different lanthanide ions (Ln^{3+}) such as Eu^{3+} and Tb^{3+} has also been

A.D. Alcantar-Mendoza ✉, F.J. Carrillo-Romo, A. García-Murillo, M.R. González-García
Particle technology, Instituto Politécnico Nacional, Centro de Investigación e Innovación Tecnológica, Azcapotzalco, Cd. Mx., 02250, México.

M. Diaz-Cruz
Instituto Politécnico Nacional, Escuela Superior de Ingeniería Química e Industria Extractivas, Gustavo A. Madero, Cd. Mx., 07700, México.

Presented at the Luminescence phenomena *Simposium*, *XVII Intl. Conf. on Surfaces, Materials, and Vacuum, SMCTSM*, September 23rd to 27th, 2024. Ensenada, BC, Mexico.
Received: September 24th, 2024.
Accepted: May 12th, 2025.
Published: May 20th, 2025.

https://doi.org/10.47566/2025_syv38_1-250501

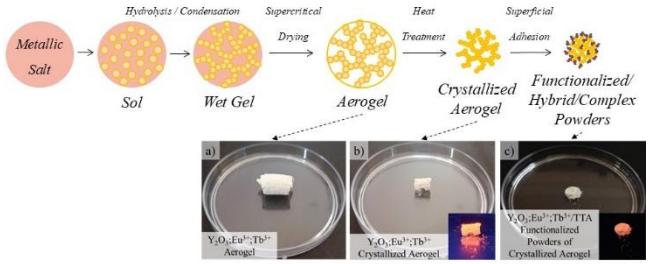

Figure 1. Diagram of the sol-gel method, from metallic salt to functionalized/hybrid/complex powders of aerogels. Images of Y_2O_3:Eu^{3+};Tb^{3+}: (a) as an aerogel, (b) as a crystallized aerogel, and (c) as Y_2O_3:Eu^{3+};Tb^{3+}/TTA, a functionalized powder made from the crystallized aerogel.

studied, with the aim of producing changes and benefiting the luminescent properties, although this research is mainly focused on generating red emissions for use in optical fibers, security operations, photo storage, lasers, LEDs, and biological markers [34-37]. Also, functionalization is the process of modifying materials and endowing them with different or new properties [38,39]. Some of the most-studied compounds used to functionalize REOs *ceramics* are affiliated with the family of β-diketones and some of their derivatives; these help with the formation of complex/hybrid/functionalized materials with the capacity to alter optical properties through the antenna effect, capturing a greater amount of energy by modifying the absorption ranges. [40-42]. Although REOs *aerogels* are a relatively new material [43-45], there are some reports on Y_2O_3 aerogels doped or co-doped with Ln^{3+} [46,47]; however, in the literature on REOs aerogels, functionalization with β-diketones is a process for which no reports are found.

For this work, three different Y_2O_3 aerogels co-doped with Eu^{3+} and Tb^{3+} ions were synthesized. They differed from each other in the molar amounts of europium used in the material, which were 2, 4, and 8 mol%, while the molar amount of terbium was low and constant (0.075 mol%). After being crystallized and analyzed the aerogels, each sample was functionalized with 9 µmol of 2-thenoyltrifluoroacetone (TTA, β-diketone compound) to be characterized and compared with the crystallized aerogels.

Experimental details

The precursors used were Y_2O_3 (Sigma Aldrich, 99.9%), Eu_2O_3 (Sigma Aldrich, 99.9%), Tb_2O_3 (Sigma Aldrich, 99.9%), HCl (Fermont, 36.7%), C_2H_6O (EtOH, 99.7%, Fermont), C_3H_6O (PO, Sigma Aldrich, 99%), $C_6H_8O_7{\cdot}H_2O$ (J. T. Baker, 100.2%), CO_2 (INFRA group), and $C_8H_5F_3O_2S$ (2-thenoyltrifluoroacetone, Sigma Aldrich, 99%). Y_2O_3:Eu^{3+};Tb^{3+} aerogels were synthesized following the methods established in [43,48], In this case yttrium oxide (Y_2O_3) was used as a matrix; 2, 4, and 8 mol% of Eu^{3+} were used for the different doping concentrations, while Tb^{3+} was incorporated as a co-dopant at the same concentration (0.075 mol%) in all three samples.

The sol-gel synthesis was based on preparing two different solutions (A and B). Solution A consisted of a mixture of the REOs precursors in HCl, stirred at 80 °C for 30 min. In solution B, citric acid was dissolved in the presence of ethanol (1:10). When solution A went from being whitish to translucent, the metal salt was obtained, and 2 mL of EtOH were added to favor the hydrolysis and condensation reactions of the sol. Then, 1.5 mL of PO were added to act as a gelation initiator, and finally 2 mL of solution B were added, which acted as a catalyst to immediately form a gel, which again looked whitish. This is the process schematized in the diagram in Figure 1.

After aging the gels for one day, the liquid phase (EtOH) contained in them was extracted under supercritical conditions reached at 73 bar and 34 °C with CO_2. The supercritical drying process was carried out in triplicate, with gas changes every hour to ensure complete extraction. At this point, the aerogels obtained (Figure 1a) were amorphous materials; they were then heat-treated at 800 °C for 2 h to obtain crystallized aerogels (Figure 1b).

Finally, functionalization of the materials was carried out by careful grinding to avoid damaging the structure of the aerogels. TTA (9 µmol) was added separately to each of the samples – Y_2O_3:Eu^{3+}(2 mol%);Tb^{3+}, Y_2O_3:Eu^{3+}(4 mol%);Tb^{3+} and Y_2O_3:Eu^{3+}(8 mol%);Tb^{3+} – resulting in functionalized powders of crystallized aerogels: Y_2O_3:Eu^{3+}(2 mol%);Tb^{3+}/TTA, Y_2O_3:Eu^{3+}(4 mol%);Tb^{3+}/TTA (shown in Figure 1c), and Y_2O_3:Eu^{3+}(8 mol%);Tb^{3+}/TTA. The general information for each sample is presented in Table 1.

Characterization techniques

The crystallographic-structural behavior was studied through x-ray diffraction (XRD) on a Bruker D8 ADVANCE diffractometer, using the powder method with a Cu-Kα radiation covering the 2θ angle of 20-80°. Also, the average size of the crystallites was calculated using the Debye Scherrer equation and the lattice parameters were calculated by Rietveld refinement. The morphological comparison was studied at a voltage of 10 kV and 50,000× in a JEOL JSM-6701F scanning electron microscope. The functional groups were identified by infrared (IR) spectroscopy, on Perkin Elmer Spectrum 65 spectrometer, using transmittance for 2 min at a wavenumber from 4000 - 400 cm^{-1}. Raman spectroscopy was performed using a Horiba confocal micro-Raman spectrometer using a diode laser excitation line with

Table 1. Compositional profiles of the crystallized and functionalized aerogel samples.

Sample name	**Content of the compounds**		
	Eu^{3+} (mol%)	Tb^{3+} (mol%)	TTA (µmol)
Y_2O_3:Eu^{3+}(2 mol%);Tb^{3+}	2	0.075	
Y_2O_3:Eu^{3+}(4 mol%);Tb^{3+}	4		
Y_2O_3:Eu^{3+}(8 mol%);Tb^{3+}	8		
Y_2O_3:Eu^{3+}(2 mol%);Tb^{3+}/TTA	2		9
Y_2O_3:Eu^{3+}(4 mol%);Tb^{3+}/TTA	4		
Y_2O_3:Eu^{3+}(8 mol%);Tb^{3+}/TTA	8		

a wavelength of 785 nm at room temperature. The photoluminescence and photoluminescence emission (PL+PLE) analysis were obtained using a Hitachi F-7000 fluorescence spectrophotometer with a 150-W xenon lamp. The spectra were recorded in accordance with the interaction intervals of the luminescent ion (Eu^{3+}), these were at wavelengths of excitation: 255 and 355 nm and emission: 612 nm. The voltage was 700 V, the slits opening was: 2.5 nm, and the analysis time for each result was 2400 nm/min. The quantum yield (QY) was calculated with a SC-30 Sphere Integrator Module on a Edinburgh Instruments FS5 spectrofluorometer and the software used for calculate the chromatic coordinates was ColorCalculator.

Results and discussion

X-ray diffraction

The results of the XRD characterization are presented in Figure 2. In all the samples, the presence of Bragg reflections can be observed, which are associated with the formation of high purity cubic-type crystalline structures (Ia3), identified after indexing with the yttrium oxide (Y_2O_3 ICSD 98-001-6394) and europium oxide (Eu_2O_3 ICSD 98-009-6953) cards.

The Bragg reflections in the diffractograms shown in Figure 2 are mainly consistent with the structure of Y_2O_3; they are located around the angles 20, 29, 33, 48, and 57, corresponding to the planes (112), (222), (004), (044), and (226), respectively. A response can be seen that indicates an absence of phase mixing, judging from the lack of peaks corresponding to some Eu phase; in this case if the concentration had been increased, a remarkable shift in the diffractions towards the Eu_2O_3 zone would have resulted. As for Tb, the equipment was not able to detect it, due to the small amount with which the co-doping was performed. The same occurred with the TTA, used in even smaller amounts. The diffractogram of the 2-thenoyltrifluoroacetone precursor confirms this; it shows an intense Bragg reflection around the angle of 25° which is not visible in any of the samples. The above could be thought of as an unfavorable result; however, it confirms that the TTA was adhered to the surface and did not cause drastic changes in the crystalline structure of the materials.

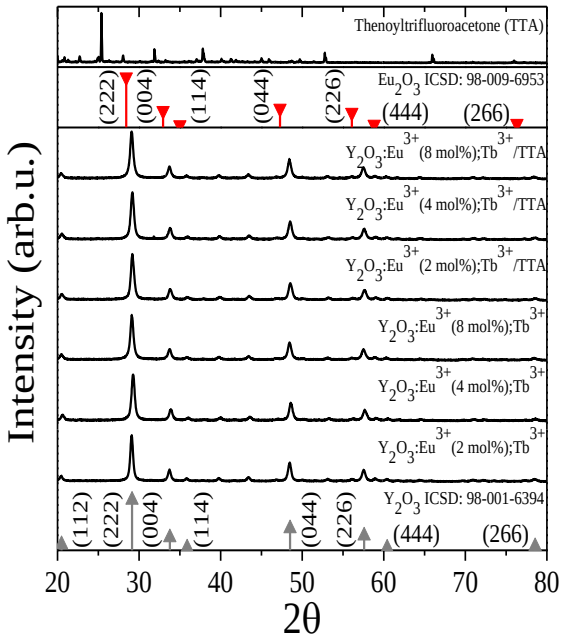

Figure 2. XRD patterns of the crystallized Y_2O_3:Eu^{3+};Tb^{3+} aerogel, functionalized powders of the crystallized Y_2O_3:Eu^{3+};Tb^{3+}/TTA aerogels, and the 2-thenoyltrifluoroacetone (TTA) precursor.

Table 2. Lattice parameters of the crystallized and functionalized aerogel samples.

Sample name	CSs (nm)	Lattice parameters			
		d Rietveld (nm)	*a/b/c [Å]*	*α/β/γ [°]*	*Volume [Å³]*
Y_2O_3:Eu^{3+}(2 mol%);Tb^{3+}	16	3.06	10.61		1196.25
Y_2O_3:Eu^{3+}(4 mol%);Tb^{3+}	16	3.05	10.62		1200.23
Y_2O_3:Eu^{3+}(8 mol%);Tb^{3+}	15	3.06	10.63		1201.81
Y_2O_3:Eu^{3+}(2 mol%);Tb^{3+}/TTA	15	3.06	10.61	90	1196.71
Y_2O_3:Eu^{3+}(4 mol%);Tb^{3+}/TTA	15	3.05	10.62		1200.08
Y_2O_3:Eu^{3+}(8 mol%);Tb^{3+}/TTA	15	3.06	10.63		1200.79

Additionally, the crystallite sizes (CSs) for each sample were determined using the Scherrer equation. From the results (see Table 2), it can be seen that all the values are between 15 and 16 nm. These values are similar to those obtained in [49] where similar Y_2O_3:Eu^{3+},Tb^{3+} nanopowders were synthesized and thermally treated. Among the advantages of the sol-gel process is the ability to "manipulate" the morphology of crystals/particles and reduce their size, which is due to the homogeneity of the sol [50].

The results indicate that neither Eu^{3+} nor Tb^{3+} distorted the lattice parameters, but were bound to the pure phase of Y_2O_3, where Ln^{3+} ions were impurities that formed the co-doping. In addition, with the use of grinding to incorporate the TTA, no changes occurred in the crystallite sizes. This is more noticeable in the results reported in Table 2, each crystallized aerogel sample presents a slight change between them, indicating a slight increase in the parameters due to the substitution of the Y^{3+} ions by Eu^{3+} or Tb^{3+}. The behavior prevailed once the crystallized aerogels were functionalized, confirming what was mentioned and expected about the fact that TTA would not have the effect to modify the network parameters since it was only added superficially.

Scanning electron microscopy (SEM) with energy dispersive spectroscopy (EDS)

The SEM analysis, whose results are shown in Figure 3, was carried out on the crystallized Y_2O_3:Eu^{3+}(4 mol%);Tb^{3+} aerogel (Figure 3a) and its functionalized counterpart Y_2O_3:Eu^{3+}(4 mol%);Tb^{3+}/TTA (Figure 3b). For the Y_2O_3:Eu^{3+}(4 mol%);Tb^{3+} sample, it can be seen that supercritical drying helped to effectively extract the solvent, allowing the aerogel particles, with sizes around 100 nm, to

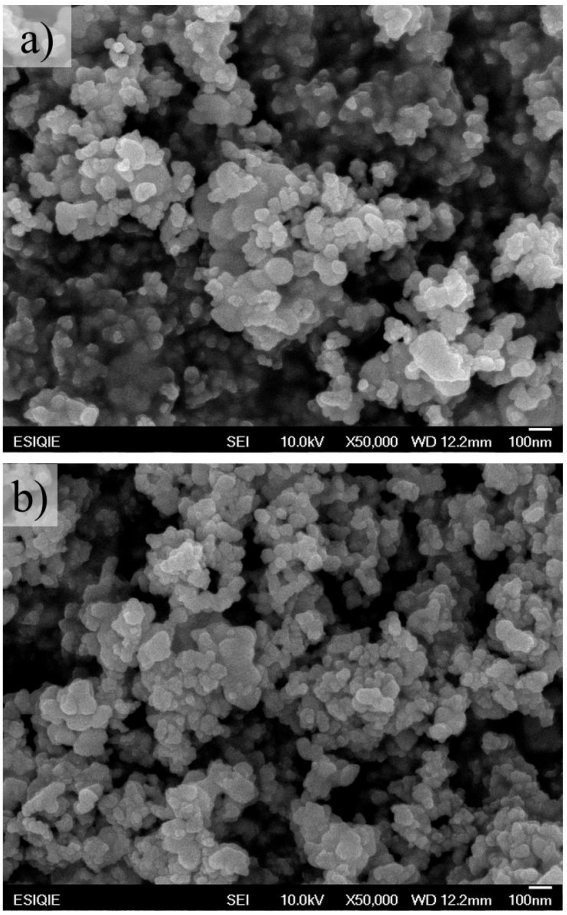

Figure 3. Scanning electron micrographs for the samples of: (a) Y_2O_3:Eu^{3+}(4 mol%);$Tb^{3+}$and (b) Y_2O_3:Eu^{3+}(4 mol%);Tb^{3+}/TTA.

remain interconnected. Although the particles were somewhat agglomerated, the space between them can be understood as the porosity associated with aerogels.

It could be expected that the micrographs would show an abrupt change in the morphology of the crystallized aerogels, due to the surface adhesion of the TTA, since the three-dimensional structure that forms the aerogels is extremely fragile and susceptible to collapse under any process, in this case, grinding. Therefore, in the case of the sample Y_2O_3:Eu^{3+}(4 mol%);Tb^{3+}/TTA, it was expected a compaction of the particles, similar to what occurred in [48], where the adhesion of TTA by grinding considerably changed the 3D network of the REOs materials, forming large particles. Despite this, it seems that no change occurred in the structure, aggregates, or size of the particles.

Infrared (IR) spectroscopy

Infrared spectra of the crystallized Y_2O_3 aerogels co-doped with Eu^{3+} and Tb^{3+} ions are shown in Figure 4a. The bands observed near 1500, and 1400 cm^{-1} correspond to the C=O vibrations associated with CO_2 molecules absorbed by the samples under ambient conditions. In addition, vibrational bands corresponding to the interaction of rare earths elements with oxygen (RE-O) located at 566 cm^{-1} are present. In the three samples of crystallized aerogels, the same bands, belonging to the RE-O vibrational modes, are

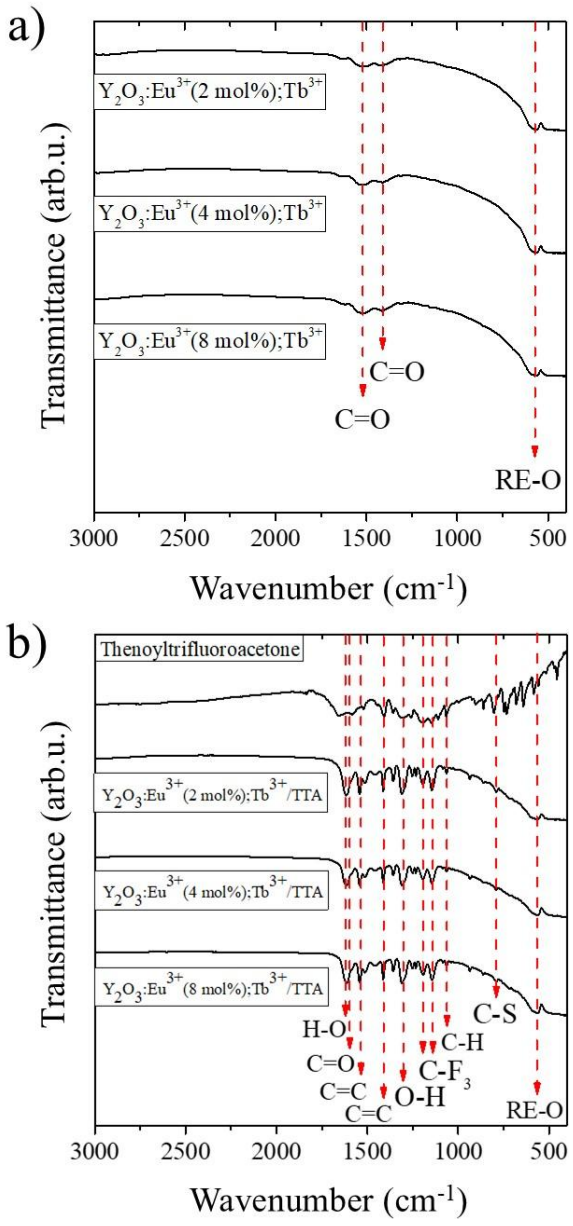

Figure 4. IR spectra of (a) the crystallized Y_2O_3:Eu^{3+};Tb^{3+} aerogels, and (b) functionalized powders of the crystallized Y_2O_3:Eu^{3+};Tb^{3+}/TTA aerogels.

observed, without any noticeable influence from the different mol% concentrations of rare earths. Given this, it is thought that the concentration of the element Tb, being constant and very low, did not cause a significant change, since as mentioned in another work [51], its main interaction has been located around 580 cm^{-1}.

This result was maintained when TTA was adhered to the crystallized aerogels in Figure 4b. However, compared to XRD, there was a significant change in that a large number of bands appeared, which have been reported in similar REOs materials to which TTA is added [42,48,52] Hence, the infrared spectrum of the precursor 2-thenoyltrifluoroacetone was also obtained (Figure 4b). With this information, it was possible to establish that the change was due to the functionalization carried out by

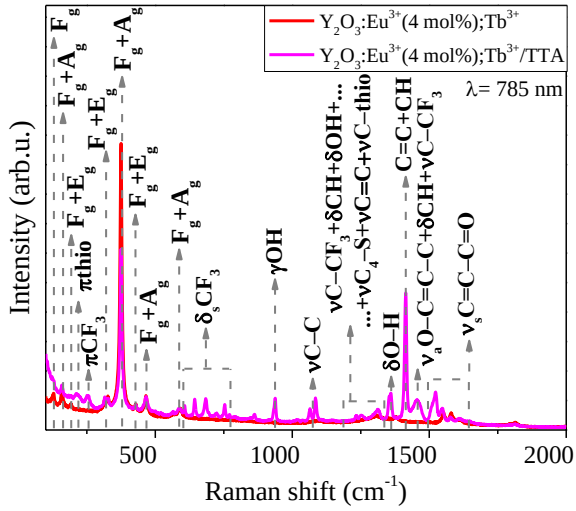

Figure 5. Raman spectra of the samples Y_2O_3:Eu^{3+}(4 mol%);Tb^{3+} and Y_2O_3:Eu^{3+}(8 mol%);Tb^{3+}/TTA excited at 785 nm.

milling, since the new bands are similar to those of the TTA precursor. Some of the main bands are as follow: around 1620, and 1300 cm^{-1} a band assigned to the vibration (O-H), resulting from the hydration of the samples; also, nearly at 1620 cm^{-1} a band assigned to the ketone group (C=O), which indicates that TTA was included superficially by the interaction of TTA with the Eu^{3+} ions; approximately at 1540 cm^{-1} a relevant band assigned to the C=C, which suggests that TTA formed complexes with the crystallized aerogels; at 1410 cm^{-1} a band in response to the stretching of the thenoyl ring (C=C); at 1190, and 1140 cm^{-1} bands associated with the (C-F_3) mode; at 1060 cm^{-1} a band attributable to the deformation of the thenoyl ring (C-H); and at 790 cm^{-1}, a band corresponding to the vibrations of the thiophene groups (C-S).

Raman spectroscopy

Figure 5 shows the Raman spectra of the samples Y_2O_3:Eu^{3+}(4 mol%);Tb^{3+} and Y_2O_3:Eu^{3+}(4 mol%);Tb^{3+}/TTA. Regarding the crystallized aerogel sample, bands related to the F_g, A_g, and E_g vibrational modes can be noticed, which are mainly located below 800 cm^{-1}. This behavior is natural because the phonon energy of REOs is low and the vibrational modes occur in this range [53]. However, once the crystallized aerogel has been functionalized, the appearance of new bands is evident, primarily in areas greater than 1000 cm-1, which correspond to the different vibrational modes due to the incorporation of the TTA compound. In the same sense as IR spectroscopy, the interactions are mainly due to the vibrations of the CF_3, C=C, OH, CH, C-S groups [54–56].

It can also be observed that the intensity of the main band at 372 cm^{-1} of the crystallized aerogel is higher than the functionalized powders of the samples doped at 4 mol%. This may be due to the efficiency of the luminescence processes by each sample, which is a first indication that the crystallized aerogel sample has a higher luminescence efficiency, but it is also evidence that TTA is being included in the chemical composition by adhesion through grinding because no drastic changes in the lattice parameters and crystallites sizes were reported in XRD section.

Photoluminescence and photoluminescence emission (PL+PLE) studies

The complete results of the luminescence studies of the synthesized samples are shown in Figure 6 and Figure 7. Figure 6a is a representation of the antenna effect that the TTA had on the Eu^{3+}-Tb^{3+} ions by "adhering" to the REOs crystallized aerogels through an ionic bond between the oxygens of the TTA and the RE-bonded particle network. Several research groups [48,52,53,57], have proposed that TTA, due to its interaction with REOs, acts as a ligand, capturing a great amount of energy by the antenna effect, absorbing them (from S_0 to S_1), causing the TTA to distribute the energy separately to each of the Ln^{3+} ions and that each one acts as a luminescence activator. TTA was expected to distribute the energy in such a way that a cooperative energy transfer between Eu^{3+} and Tb^{3+} would occur by distributing the energy to the Tb^{3+} sublevel ($^5D_4$), so that it acts as a sensitizer; concentrating the energy to the $^5D_0$ sublevel of Eu^{3+}, where the energy will relax until returning to the 7F sub-levels, which finally acts as a luminescence activator. This is schematized by the energy conversion diagram in Figure 6b.

In this sense, the excitation-emission spectra obtained for the crystallized aerogels (Y_2O_3:Eu^{3+};Tb^{3+}) in the range from 200 to 720 nm are first shown in Figure 7a. When examining the 612 nm band, which corresponds to the main

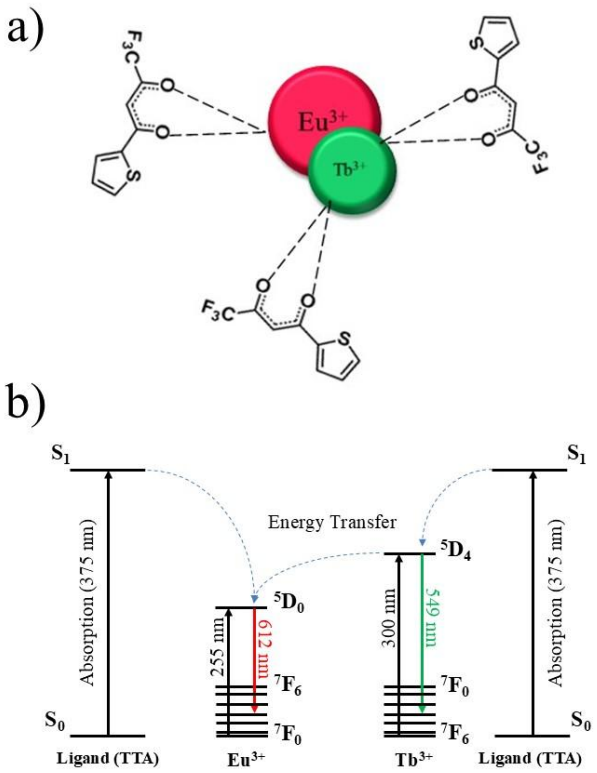

Figure 6. (a) Representation of the antenna effect of TTA on the Eu^{3+};Tb^{3+} ions, and (b) energy transfer diagram for the Eu^{3+};Tb^{3+}/TTA system.

hypersensitive transition of Eu^{3+} ion ($^5D_0$-$^7F_2$) [58], caused by the C_2 sites in the cubic lattice of Y_2O_3 [49], different bands appear. One of great intensity around 255 nm can be attributed to the O^{2-}-Eu^{3+} interaction, another of much lower energy at 300 nm to the O^{2-}-Tb^{3+} interaction, and others between 310 nm and 400 nm to the F transitions of the Eu^{3+} ion. When using the wavelength (WL) corresponding to O^{2-}-Eu^{3+} absorption (255 nm), a series of low intensity bands were observed, assigned to the transitions $^5D_4$-$^7F_5$ (between 535-560 nm) and $^5D_4$-$^7F_3$ (around 620 nm), which are characteristic of the Tb^{3+} ion. The possibility of an overlap between the missing Tb^{3+} transitions with those of the Eu^{3+} ion cannot be ruled out, which showed its transitions: $^5D_0$-$^7F_0$ (around 580 nm), $^5D_0$-$^7F_1$ (around 590 nm), $^5D_0$-$^7F_2$ (peaking at 612 nm), $^5D_0$-$^7F_3$ (at 650 nm), and $^5D_0$-$^7F_4$ (at 710 nm). These responses were the same for all the samples; however, there was a noticeable difference in the luminescence intensity of the crystallized aerogel that was co-doped with 4 mol% of europium (Figure 1b). This enhancement is attributable to the sensitization resulting from the high energy absorption of Tb^{3+} that results in a nonradiative cooperative energy transfer of Tb^{3+} to Eu^{3+} [59,60]. The sample Y_2O_3:Eu^{3+}(8 mol%);Tb^{3+} presented the least intense luminescence, while the sample Y_2O_3:Eu^{3+}(2 mol%);Tb^{3+} remained intermediate.

Once the samples were functionalized with TTA and the crystallized aerogel powders were obtained (Y_2O_3:Eu^{3+};Tb^{3+}/TTA), excitation-emission spectra were obtained in the same range, from 200 to 720 nm (Figures 7b and 7c). Again, in Figure 7b the primary focus was on the $^5D_0$-$^7F_2$ transition (612 nm), featuring energy absorption by the O^{2-}-Eu^{3+} (255 nm) and O^{2-}-Tb^{3+} (300 nm) interactions, although for this samples, when the TTA was adhered, the F transitions were overlapped by a broad band corresponding to the absorption of the ligand (TTA), with a maximum at 375 nm. In this case, a WL of 255 nm (O^{2-}-Eu^{3+}) was used to generate the emission, which caused the transitions of the Tb^{3+} ion, $^5D_4$-$^7F_5$ and $^5D_4$-$^7F_3$, continued to appear although they were even less intense. This behavior is similar to that observed in the research of Ji *et al.* [52], and Yu *et al.* [53]. However, in the case of Eu^{3+}, only the transitions $^5D_0$-$^7F_0$, $^5D_0$-$^7F_1$, and $^5D_0$-$^7F_2$ appeared, also at a lower intensity, which could be due to the low absorption from the O^{2-}-Eu^{3+} interaction when TTA is present.

However, for the same Y_2O_3:Eu^{3+};Tb^{3+}/TTA samples, when using the WL assigned to the ligand absorption band (375 nm), a more favorable emission response was obtained (Figure 7c) by inducing the energy transfer depicted in Figure 6b, finding the same transitions were found as for the crystallized aerogels (Figure 7a). Although some differences are seen in the emission bands, the $^5D_0$-$^7F_2$ transition at 612 nm remains the representative band. Moreover, another appreciable effect when functionalizing the crystallized aerogels with TTA was a change in the intensity of the emissions; the sample Y_2O_3:Eu^{3+}(8 mol%);Tb^{3+}/TTA (Figure 1c) exhibiting a better response to the antenna effect.

It should be noted that although all the samples exhibited luminescence and did not suffer a total quenching that would completely stop the emission, in the case of the crystallized

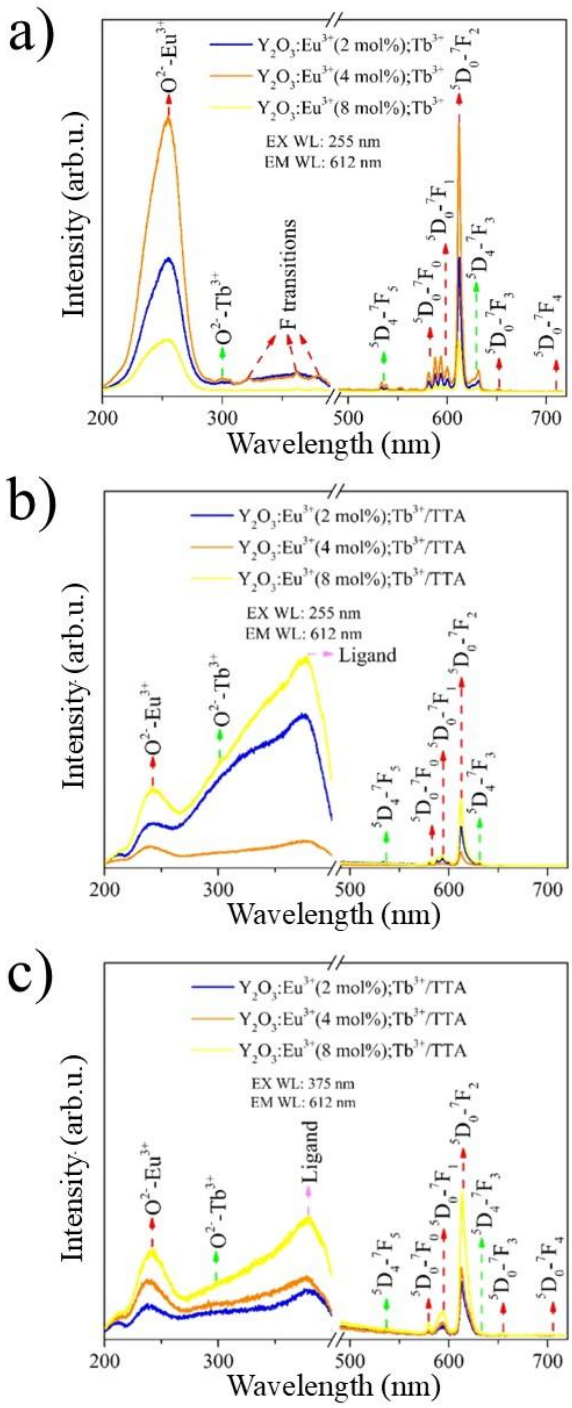

Figure 7. (a) The excitation-emission spectra of the crystallized Y_2O_3:Eu^{3+};Tb^{3+} aerogels (WL: 255 nm), (b) the excitation-emission spectra of the functionalized powders of the crystallized Y_2O_3:Eu^{3+};Tb^{3+}/TTA aerogels (WL: 255 nm), and (c) the excitation-emission spectra of the functionalized powders of the crystallized Y_2O_3:Eu^{3+};Tb^{3+}/TTA aerogels (WL:375 nm).

aerogels, the emission of the sample with 4 mol% of Eu^{3+} is prominent, and among the functionalized powders, the emissions of the sample with 8 mol% of Eu^{3+} stands out. Observing the graph in Figure 8a, this behavior is perceptible by the maximum intensities reached by the $^5D_0$-$^7F_2$ transition of each sample and at each excitation wavelength. The response of the crystallized aerogels (255 nm) suggests that

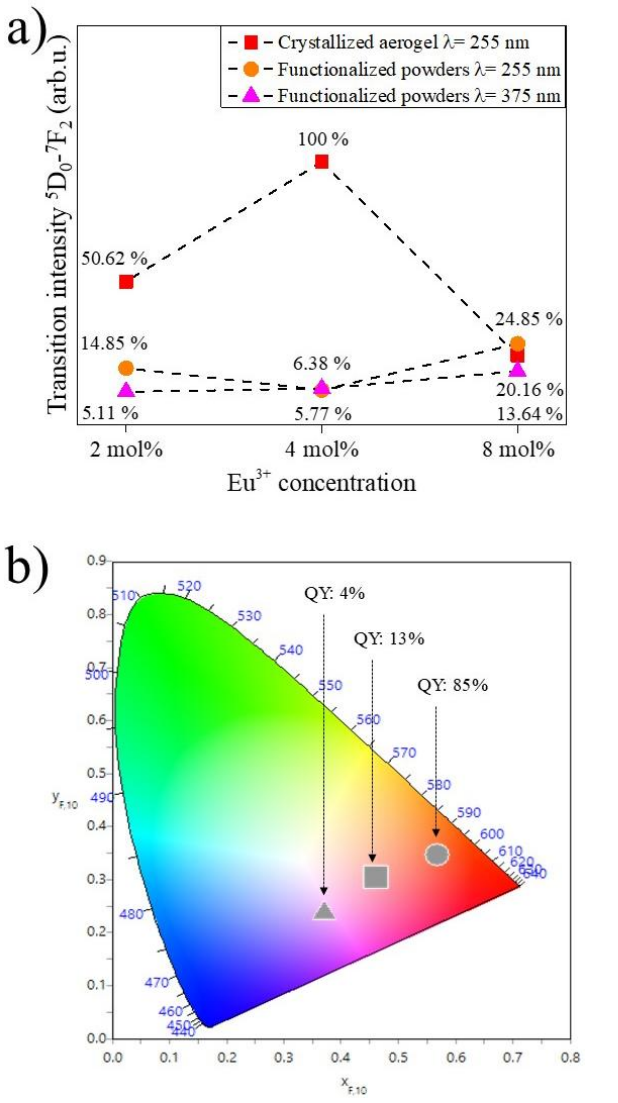

Figure 8. (a) Maximum intensity of the $^5D_0$-$^7F_2$ transition of the crystallized Y_2O_3:Eu^{3+};Tb^{3+} aerogels, and (b) CIE locations of the samples with the highest luminescence intensity.

tempering begins from 4 mol%, that the powders functionalized by the excitation of 255 nm is irregular and that when exciting at 375 nm the samples present an exponential behavior, in this sense perhaps the antenna effect could enhance the emission of Eu^{3+} by increasing its mol% concentration. concentration.

Finally, the chromatic coordinates of the samples were calculated to obtain their location in the CIE diagram (see Figure 8b). There, the circle corresponds to the sample Y_2O_3:Eu^{3+}(4 mol%);Tb^{3+}, which is located in a reddish-orange position achieving an efficient quantum yield of 85 %; the square corresponds to the functionalized sample Y_2O_3:Eu^{3+}(8 mol%);Tb^{3+}/TTA when the O^{2-}-Eu^{3+} absorption WL of 255 nm was used – its emission was shifted from reddish-orange to a pink which decreased its quantum yield to 13 %; and the rhombus represents the coordinates of the sample Y_2O_3:Eu^{3+}(8 mol%);Tb^{3+}/TTA when the absorption WL of the TTA ligand (375 nm) was used – it emission was pink-purple with a quantum yield of 4 %. It can be argued that the TTA produced an antenna effect, both on the Tb^{3+} ions and on the Eu^{3+} ions, since a change in the emission colors of the samples is apparent, due to their different absorption levels and luminescent responses.

Conclusions

According to the spectroscopic results, the functionalization of TTA by milling on the crystallized Y_2O_3:Eu^{3+};Tb^{3+} aerogels was performed properly, without any drastic changes in the structural conditions and/or morphology after TTA adhesion. Although the luminescence arising from the interaction of the Tb^{3+} sensitizer with the Eu^{3+} activator was undoubtedly intense and efficient, the antenna effect of TTA caused changes in the luminescence, shifting the quantum yields and locations of the emission colors on the chromatic coordinates. However, the $^5D_0$-$^7F_2$ transition characteristic of the Eu^{3+} ion was always predominant. Therefore, sol-gel synthesis allows obtaining aerogels that can be subjected to different processes to modify the properties of materials, in this case the luminescence of REOs aerogels, which could have biomedical applications or in optoelectronic devices and security systems, taking advantage of the benefits of functionalization with 2-thenoyltrifluoroacetone.

Acknowledgements

The authors gratefully acknowledge the financial support of this work by CONAHCYT project A1-S-28234, and by the Instituto Politécnico Nacional through SIP-IPN projects 20241486 and 20241489. The authors thank CNMN-IPN, ESIQIE, CICATA and Lab CREA CIITEC IPN for their experimental support. Alcantar-Mendoza and González-García acknowledges CONAHCYT for their PhD scholarship and Sociedad Mexicana de Ciencia y Tecnología de Superficies y Materiales A.C. for the grant awarded to attend the XVII International Conference on Surfaces, Materials, and Vacuum (XVII-ICSMV). The authors also would like to thank Henry Jankiewicz for the editing work that he did for this paper, and M. García Murillo for her assistance.

References

[1]. J. Zhou, J.L. Leaño, Z. Liu, D. Jin, K-L. Wong, R-S. Liu, J-C.G. Bünzli, *Small* **14**, 1 (2018).
[2]. T. Cheisson, E.J. Schelter, *Science* **363**, 1 (2019).
[3]. C. Huang, X. Chen, Z. Xue, T. Wang, *Sci. Adv.* **6**, 20 (2020).
[4]. B. Zheng, J. Fan, B. Chen, X. Qin, J. Wang, F. Wang, R. Deng, X. Liu, *Chem. Rev.* **122**, 6 (2022).
[5]. S. Li, L. Zhou, H. Zhang, *Light Sci. Appl.* **11**, 1 (2019).
[6]. M.R. Carro-Temboury, R. Arppe, T. Vosch, T.J. Sørensen, *Sci. Adv.* **4**, 1 (2018).
[7]. Z. Chen, G. Dong, G. Barillaro, J. Qiu, Z. Yang, *Prog. Mater. Sci.* **121**, 1 (2021).
[8]. M.K. Hossain, M.H. Ahmed, M.I. Khan, M.S. Miah, S. Hossain, *ACS Appl. Electron. Mater.* **3**, 10 (2021).
[9]. Z. Luo, D. Mao, X. Li, J. Luo, C. Gong, X. Liu, *Coord. Chem. Rev.* **508**, 1 (2024).
[10]. H. Huang, J.J. Zhu, *Analyst.* **144**, 1 (2019).
[11]. F. Tommasi, P.J. Thomas, G. Pagano, G.A. Perono, R. Oral,

D.M. Lyons, M. Toscanesi, M. Trifuoggi, *Arch. Environ. Contam. Toxicol.* **81**, 4 (2021).
[12]. B.J. Clapsaddle, B. Neumann, A. Wittstock, D.W. Sprehn, A.E. Gash, J.H. Satcher, R.L. Simpson, M. Baümer, *J. Sol-Gel Sci. Technol.* **64**, 1 (2012).
[13]. Y. He, W. Zhou, J. Xu, *ChemSusChem.* **15**, 12 (2022).
[14]. S.E. Crawford, P.R. Ohodnicki, J.P. Baltrus, *J. Mater. Chem. C* **8**, 1 (2020).
[15]. A. Kumar, N. Yadav, M. Bhatt, N.K. Mishra, P. Chaudhary, R. Singh, *Res. J. Chem. Sci.* **5**, 12 (2020).
[16]. P. Innocenzi, *Open Ceram.* **16**, 1 (2023).
[17]. L. Su, M. Niu, D. Lu, Z. Cai, M. Li, H. Wang, *J. Mater. Sci. Technol.* **75**, 1 (2021).
[18]. F. Rechberger, M. Niederberger, *Nanoscale Horizons* **2**, 1 (2017).
[19]. P. Rusch, D. Zámbó, N.C. Bigall, *Acc. Chem. Res.* **53**, 10 (2020).
[20]. M.A. Aegerter, N. Leventis, M. Koebel, S.A. Steiner, *Springer Handbook of Aerogels*, vol. 1 (Springer, Switzerland, 2023).
[21]. C.A. García-González, M.C. Camino-Rey, M. Alnaief, C. Zetzl, I. Smirnova, *J. Supercrit. Fluids* **66**, 1 (2012).
[22]. I. Smirnova, *J. Supercrit. Fluids* **106**, 1 (2015).
[23]. S. Sakka, *J. Sol-Gel Sci. Technol.* **102**, 20 (2022).
[24]. D. Bokov, A. Turki, S. Chupradit, W. Suksatan, M. Javed, I.H. Shewael, G.H. Valiev, E. Kianfar, *Adv. Mater. Sci. Eng.* **201**, 1 (2021).
[25]. D. Navas, S. Fuentes, A. Castro-Alvarez, E. Chavez-Angel, *Gels* **7**, 4 (2021).
[26]. E. Barrios, D. Fox, Y. Y. Li, R. Catarata, J.E. Calderon, N. Azim, S. Afrin, Z. Zhang, L. Zhai, *Polymers (Basel)* **11**, 4 (2019).
[27]. A.C. Pierre, M. Pajonk, *Chem. Rev.* **102**, 1 (2002).
[28]. H. Cai, Y. Jiang, J. Feng, S. Zhang, F. Peng, Y. Xiao, L. Li, J. Feng, *Mater. Des.* **191**, 1 (2020).
[29]. S. He, Y. Huang, G. Chen, M. Feng, H. Dai, B. Yuan, X. Chen, *J. Hazard. Mater.* **362**, 1 (2019).
[30]. Z. Lun, L. Gong, Z. Zhang, Y. Deng, Y. Zhou, Y. Pan, X. Cheng, *Gels* **8**, 3 (2022).
[31]. Y. Jin, H. Zhou, D. Zhang, *Rare Met. Mater. Eng.* **45**, 11 (2016).
[32]. L.L. Santos, R.C. de Lima, M.A. Schiavon, R.R. Gonçalves, H.P. Barbosa, J.L. Ferrari, *J. Lumin.* **222**, 1 (2020).
[33]. A.A. Ansari, M.A. M. Khan, S. Ameen, *J. Nanoparticle Res.* **25**, 9 (2023).
[34]. X. Wang, J. Xu, J. Yu, Y. Bu, J. Marques-Hueso, X. Yan, *Phys. Chem. Chem. Phys.* **22**, 1 (2020).
[35]. V.V. Utochnikova, *Coord. Chem. Rev.* **398**, 1 (2019).
[36]. K. Thomas, D. Alexander, S. Sisira, S. Gopi, P.R. Biju, N.V. Unnikrishnan, C. Joseph, *Opt. Mater.* **80**, 1 (2018).
[37]. A. Valladares-Barrera, A.D. Alcantar-Mendoza, A. García-Murillo, L.M. Palacios-Lazcano, F.J. Carrillo-Romo, *J. Sol-Gel Sci.* **113**, 1 (2024).
[38]. J.C.G. Bünzli, *Eur. J. Inorg. Chem.* **2017**, 44 (2017).
[39]. A. Escudero, A.I. Becerro, C. Carrillo-Carrión, N.O. Núñez, M.V. Zyuzin, M. Laguna, D. González-Mancebo, M. Ocaña, W.J. Parak, *Nanophotonics* **6**, 5 (2017).
[40]. D. Paderni, L. Giorgi, V. Fusi, M. Formica, G. Ambrosi, M. Micheloni, *Coord. Chem. Rev.* **429**, 1 (2021).
[41]. M.A. Lutoshkin, A.I. Petrov, Y.N. Malyar, A.S. Kazachenko, *Inorg. Chem.* **60**, 5 (2021).
[42]. G.L. Jiménez, M.J. Rosales-Hoz, M.A. Leyva, J.L. Reyes-Rodríguez, U. Galindo-García, C. Falcony, *J. Mol. Struct.* **1228**, 1 (2021).
[43]. M.A. Worsley, J. Ilsemann, Th.M. Gesing, V. Zielasek, A.J. Nelson, R.A.S. Ferreira, L.D. Carlos, A.E. Gash, M. Bäumer, *J. Sol-Gel Sci. Technol.* **89**, 1 (2018).
[44]. S.V. Kameneva, Kh.E. Yorov, R.K. Kamilov, S.Yu. Kottsov, M.A. Teplonogova, T.V. Khamova, M.A. Popkov, I.V. Tronev, A.E. Baranchikov, V.K. Ivanov, *J. Sol-Gel Sci. Technol.* **107**, 1 (2023).
[45]. W. Zhang, Y. Liu, H. Yu, X. Dong, *J. Photochem. Photobiol. A Chem.* **379**, 1 (2019).
[46]. A. García-Murillo, F.J. Carrillo-Romo, J. Oliva-Uc, T.A. Esquivel-Castro, S.D. Torre, *Ceram. Int.* **43**, 1 (2017).
[47]. W. Cheng, F. Rechberger, M. Niederberger, *ACS Nano* **10**, 2 (2016).
[48]. A. García-Murillo, A.D. Alcantar-Mendoza, F.J. Carrillo-Romo, I.C. Romero-Ibarra, I.A. Garduño-Wilches, *Bull. Mater. Sci.* **47**, 3 (2024).
[49]. F.D.J. Carrillo, Á.D.J. Morales, A.G. Murillo, M.G. Hernández, D.J. Vigueras, V.G. Febles, *Int. J. Mater. Res.* **103**, 10 (2012).
[50]. A. Tshikovhi, L.F. Koao, T.D. Malevu, E.C. Linganiso, T.E. Motaung, *Results Mater.* **19**, 1 (2023).
[51]. A.D. Alcantar-Mendoza, A. García-Murillo, F.J. Carrillo-Romo, J. Ortiz-Landeros, *From Doping to Mixed Phases of Y_2O_3/Tb_2O_3 Powders.* In: *Trends and Challenges in Multidisciplinary Research for Global Sustainable Development*, A.M. Hernández, K. Marcos, L.D. Canales, M. Zea, R.E. Sánchez (Springer, 2020) p. 170-180.
[52]. L. Ji, N. Chen, G. Du, M. Yan, W. Shi, *Ceram. Int.* **40**, 2 (2014).
[53]. L. Yu, J. Gao, Z. Zeng, Y. Zheng, *Chem. Pap.* **75**, 3 (2021).
[54]. A.R. Nekoei, S.F. Tayyari, M. Vakili, S. Holakoei, A.H. Hamidian, R.E. Sammelson, *J. Mol. Struct.* **932**, 1 (2009).
[55]. S. Dolai, S.K. Bhunia, L. Zeiri, O. Paz-Tal, R. Jelinek, *ACS Omega* **2**, 12 (2017).
[56]. V. Tsaryuk, V. Zolin, J. Legendziewicz, R. Szostak, J. Sokolnicki, *Spectrochim. Acta - Part A Mol. Biomol. Spectrosc.* **61**, 1 (2005).
[57]. L. Su, X. Liu, Q. Niu, Z. Li, *J. Mater. Chem. C* **12**, 1 (2024).
[58]. K. Binnemans, *Coord. Chem. Rev.* **295**, 1 (2015).
[59]. J. Li, L. Lin, W. Jiang, Z. Zhang, X. Zhang, M. Kuang, J. Zhuang, Q. Zhang, H. Ni, J. Shi, *J. Alloys Compd.* **885**, 1 (2021).
[60]. B. Shao, X. Zhang, S. Sang, A. Guo, F. Cui, X. Yang, *Eur. Polym. J.* **147**, 1 (2021).

The results included in this article were presented at the *Luminescence phenomena Simposium, of the XVII International Conference on Surfaces, Materials, and Vacuum, SMCTSM*, September 23rd to 27th, 2024. Ensenada, BC, Mexico. (see Editorial Note https://doi.org/10.47566/2024_syv37_0-240001).